Original Article

Institution of MECHANICAL ENGINEERS
Journal of ENGINEERING TRIBOLOGY

Proc IMechE Part J:
J Engineering Tribology
0(0) 1–17

DOI: 10.1177/1350650118788755
journals.sagepub.com/home/pij
SAGE

A fretting finite element investigation of a plane-strain cylindrical contact of Inconel 617/Incoloy 800H at room and high temperatures

Huaidong Yang and Itzhak Green

Abstract

This work presents a finite element study of a 2D plane strain fretting model of a half-cylinder in contact with a flat block under oscillatory tangential loading. The two bodies are deformable and are set to Inconel 617 and Incoloy 800H at room temperature (20 °C) and 800 °C. However, because the results are normalized, they can characterize a range of contact scales (micro to macro). Different coefficients of friction are used at the interface. This work finds that the edges of the contacting areas experience large von Mises stresses along with significant residual plastic strains, while pileup could also appear when the coefficients of friction are sufficiently large. In addition, junction growth is investigated, showing that the direction of the growth is in the same direction of the tangential force that the weaker material (Incoloy alloy 800H) experiences. The fretting loop (caused by the tangential force during the fretting motion) for the initial few cycles of loading is generated, and it compares well with the reported experimental results. The different extents of damage at room temperature and 800 °C are also compared.

Keywords

Contact mechanics, finite element method/analysis, fretting, friction and wear, mechanical properties, mechanics

Date received: 5 January 2018; accepted: 16 June 2018

Introduction

Fretting occurs when two contacting surfaces experience small amplitude of oscillatory relative motion under normal load. Depending on whether a stick area exists or not, the steady-state fretting regimes can be divided into partial slip and gross slip. The partial slip condition is mainly responsible for the mechanical failure of surface crack initiation and propagation, while the gross slip conditions introduce wear.[1] Fretting damage can significantly reduce the operational lifetime of components in nuclear reactors, including valve stems and seats, control rod drive mechanisms, fuel handling mechanisms, and helium circulators. In particular, fretting damage of steam generator tube materials in the nuclear plants can lead to the leakage of the primary cooling water.[2]

Incoloy alloy 800H (ALLOY 800H) and Inconel alloy 617 (ALLOY 617) are promising structural materials for high temperature and very high-temperature gas-cooled reactors (HTGRs/VHTRs); they possess excellent high-temperature thermo-mechanical properties and also offer environmental protection. These two materials are the subjects for the analysis in this work.

The fretting phenomenon has been thoroughly investigated experimentally. The first experimental work can be traced back to Courtney-Pratt and Eisner.[3] They studied a sphere-over-flat contact between metallic materials under oscillatory tangential force. They also focused on the initial stage of the oscillatory tangential load but do not include the wear and fatigue caused by thousands of cycles of load. The junction growth, i.e. increase in the contact area, and also the hysteresis loops of tangential force are reported. The junction growth under the fretting load condition was also reported by Tabor,[4] and by Parker and Hatch.[5] Following the study with initial fretting cycles, fretting wear and fatigue are studied experimentally.[6–8] The fretting in Leonard et al.[6] occurs on the coating material of tungsten carbide

Georgia Institute of Technology, G. W. Woodruff School of Mechanical Engineering, Atlanta, GA, USA

Corresponding author:
Itzhak Green, Georgia Institute of Technology, G. W. Woodruff School of Mechanical Engineering, Atlanta, GA 30332-0405, USA.
Email: green@gatech.edu

reinforced amorphous hydrocarbon (WC/a-C: H) and chromium nitride (Cr2N). Warhadpande et al.[8] studied the effect of fretting wear on the contact fatigue life of M50 bearing steel. The studies of Kim and Lee,[9] Kim et al.,[10] and Zhang et al.[11] focus on the fretting damage for materials applied in the steam generator, including Inconel 600, Inconel 690, and Incoloy 800.

Although sufficient experimental work has been done on fretting, the theoretical analysis lacks the modeling of fretting at the regimes of elastic-plastic and fully plastic contacts, especially for cylindrical contacts. The elastic-plastic and fully plastic spherical contacts in strictly normal loading have been studied in great detail, using the finite element analysis (FEA) method.[12–14] The elastic-plastic cylindrical contact in plane stress was recently done by Sharma.[15] However, when the tangential force is introduced under normal load, few attempts to analyze the contact have been made. Brizmer et al.[16] use finite element method to investigate the spherical contact under the fully stick condition with tangential load. Junction growth is reported in all regimes of contact, elastic, elastic-plastic, and plastic. Chang and Zhang[17] model their contact without fully stick conditions and apply static frictional coefficient. Similar results of junction growth are found in the elastic-plastic regime. The work by Boucly et al.[18] presented a semi-analytical method for the tridimensional elastic-plastic sliding contact between two hemispherical asperities using either a load-driven or a displacement-driven algorithm. The contact pressure distribution, the hydrostatic pressure, and the equivalent plastic strain state below the contacting surfaces are found. Pile-up induced by the permanent deformation of the bodies due to their relative motion is evident. A similar pile-up phenomenon is also present in the current work.

However, cylindrical contact, which is the prototype of contacts in gears, rolling element bearings, wheel on rail and human joints, is not considered in the above work. The work by Vijaywargiya and Green[19] presented the results of FEA used to simulate two-dimensional (2D) sliding between two interfering elastic-plastic cylinders. The material for the cylinders is modeled as elastic-perfectly plastic and follows the von Mises yield criterion. The FEA provides trends in the deformations, reaction forces, stresses, and net energy losses as a function of the interference and sliding distance between the cylinders. Results are presented for both frictionless and frictional sliding and comparisons are drawn. The effects of plasticity and friction on energy loss during sliding are also given. However, while Vijaywargiya and Green[19] does analyze the elastic-plastic damage done in the tugging of interfering bodies one across the other, sliding is applied in one direction only, i.e. the repetitive (back-and-forth) fretting motion is not analyzed. The only works found so far of parallel cylindrical fretting contact are that of Gupta et al.[20] and Ghosh et al.[21] Specifically, Gupta et al.[20] model consists of a meagre 285 elements, which is limited by the computational memory typically available in 1993. Ghosh et al.[21] simulated fretting wear of Hertzian line contact in partial slip. The materials are not for steam generators and the results are not presented in a nondimensional form. Mei et al.[2] investigated the cylindrical fretting wear via FEA for the material, Inconel 690 alloy, which is used for steam generator in nuclear power plants. However, the stress field distribution, the effects of the COF, normal load, and plastic deformation are not considered. With current computing capabilities, the accuracy of these results can be improved considerably and that is one of the aims of this work. First, modeling is performed with sufficiently fine and adaptive meshes that capture the behavior in the contact region with great accuracy. Then, the materials in simulation are those used in steam generators, and the results are reported in a nondimensional form to allow their broader utility. Lastly, this work examines the effects of the COF, highly elevated temperatures, and the normal load on the fretting damage. Similar to the current work, the fretting analysis between identical steel materials in plane strain cylindrical contacts is done in Yang and Green.[22] Some of those results will be used herein.

Fretting can happen under specified loads, specified displacements, or a combination of both. The outcomes of displacement-controlled and load-controlled fretting are different in wear tests according to Mohrbacher et al.[23] Displacement-controlled fretting is applicable to conditions when the contacting elements are confined within prescribed spaces, such as prosthetic knee joints,[24–26] bolted joints and interference (press) fits,[27,28] and cutting tools in machining.[29] Therefore, the understanding of displacement-controlled fretting is useful for these and like applications including steam generators, and it is, hence, the impetus of this work.

In this work, the finite element approach, using ANSYS17.1, is applied to analyze the fretting damage for a 2D plain strain contact between a half-cylinder and a flat block of materials Inconel 617 and Alloy 800H at room temperature and 800 °C. The model is a half-cylinder in contact with a flat block. As shown in Figure 1, the loading inputs are a vertical interference, ω, and a following oscillatory horizontal displacement, δ, forced upon the cylinder while the block is held fixed. The said normal interference and horizontal displacement generates corresponding reactions P and Q, respectively, which are outputs obtained from the FEA results. The normal loading is done in the elastic-plastic regime. The development of the von Mises stresses and plastic strains near the contacting surfaces, the junction growths, the evolution of the tangential forces in the initial few cycles of oscillatory tangential loads, and the scars on the surface of the block are obtained. The effects of the COFs and the normal

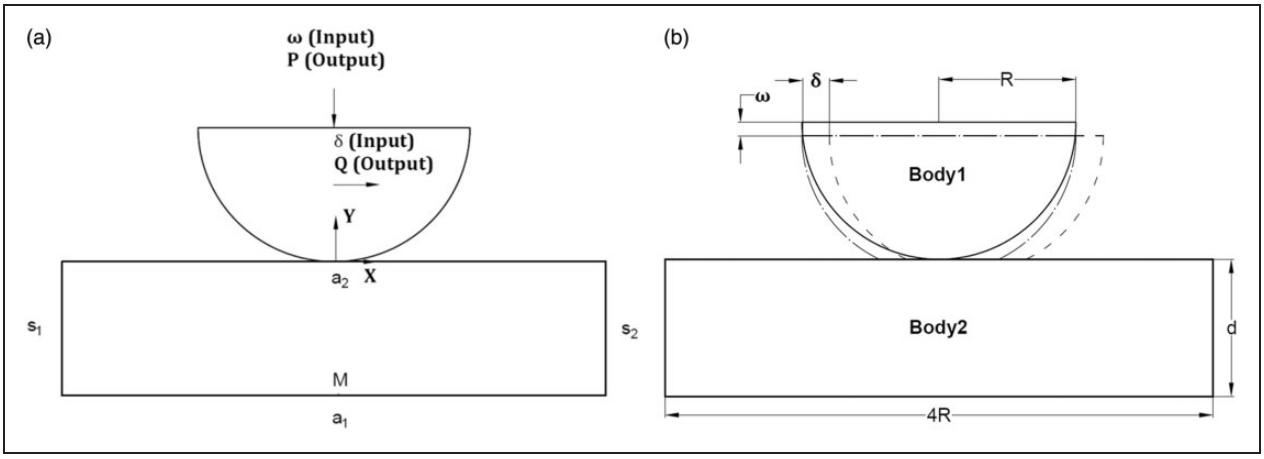

Figure 1. Schematic of a half-cylinder in contact with a flat block, along with the loading definitions: (a) displacement-controlled inputs and reaction outputs; (b) cylinder-block dimensions and displacement directions.

Table 1. Material properties of Inconel alloy 617 and Incoloy alloy 800H at 20 °C and 800 °C, and steel at 20 °C.[22]

Temperature	Material	Elastic modulus, E (GPa)	Yielding strength, S_y (MPa)	Poisson's ratio, ν	$C(\nu)$	$C{\cdot}S_y$ (MPa)
20 °C	ALLOY 617	211.0	322	0.3	1.795	578
	ALLOY 800H	196.5	150	0.339	1.839	276
800 °C	ALLOY 617	157.0	290	0.3	1.795	521
	ALLOY 800H	141.3	90	0.394	1.839	170
20 °C	Steel [22]	200	911.5	0.32	1.818	1657

interferences on the block are also investigated. The results of this work agree well with the former related experimental data. The objective is to form an in-depth understanding of the mechanisms of fretting wear, and the propensity for crack initiation and propagation.

The model

Figure 1(a) presents a half-cylinder of a radius $R = 0.5\,\text{m}$ in contact with a $4\,\text{R} \times \text{R}$ block. In the figure, the axes of X and Y are shown where the origin is located at the initial contact point. The four sides of the block are represented by a_1, a_2, s_1, and s_2.

The materials of the two bodies are special alloys, ALLOY 800H and ALLOY 617. The material properties of the alloys at room temperature and 800 °C are listed in the Product Handbook,[30] and summarized in Table 1. The data for steel is taken from Yang and Green.[22] The yield strength of ALLOY 800H is about half of that of ALLOY 617 at room temperature. The parameter $C(\nu)$ represents the ratio between the maximum pressure and the maximum von Mises stress in normal elastic contact as given by Green.[31] The elastic-perfectly plastic behavior is used in the FEA. Adhesion is not included in this work.

The fretting model is now introduced. As shown in Figure 1(b), the cylinder radius is R, where the block dimensions are given in terms of the radius, and are maintained so throughout this work. First, a vertical displacement, ω, is applied on the top of the half-cylinder. That is referred to as the interference. While keeping the interference constant, horizontal oscillations, δ, are then applied to simulate the fretting motion. That is, the top of the half-cylinder is forced to displace a certain distance to the right and then back to the left passing the origin position, continuing the same distance to the left before returning back to the origin—that constitutes one cycle of loading. The procedure is performed quasi-statically, taking 40 load steps within ANSYS to complete one cycle. Referring motion to the "right" or to the "left," metaphorically indicates motion in the positive or negative X-axis, respectively.

In an elastic contact regime, the solution of the 2D plane strain cylindrical contact is given by the Hertzian contact model. Under a total load per unit length, P/L, the maximum pressure, p_0, is located at the center of the contact[32]

$$p_0 = \frac{2P}{\pi b L} \tag{1}$$

The half-width of the contact, b, is given by

$$b = \left(\frac{4PR}{\pi LE'}\right)^{\frac{1}{2}} \tag{2}$$

where E' the equivalent elastic modulus is given as

$$\frac{1}{E'} = \frac{1-\nu_1^2}{E_1} + \frac{1-\nu_2^2}{E_2} \tag{3}$$

In equation (3), E_1 and ν_1 represent the elastic modulus and Poisson's ratio of the cylinder, while E_2 and ν_2 represent the elastic modulus and Poisson's ratio of the block. The interference of a half-cylinder in contact with a block, whose depth is d, is derived in Appendix 1

$$\begin{aligned}\omega = {} & \frac{P}{L}\frac{(1-\nu_1^2)}{\pi E_1}\left\{\ln\left(\frac{4\pi E'R}{P/L}\right) - 1\right\} \\ & + \frac{P}{L}\frac{(1-\nu_2^2)}{\pi E_2}\left\{\ln\left(\frac{\pi d^2 E'}{RP/L}\right) - \frac{\nu_2}{(1-\nu_2)}\right\}\end{aligned} \tag{4}$$

According to Green,[31] the ratio between the maximum pressure and the maximum von Mises stress in normal elastic contact is defined by $C(\nu) = p_o/\sigma_{e-\max}$. At the onset of yielding $\sigma_{e-\max} = S_y$. For contact between dissimilar materials, the minimum of C_1S_{y1} and C_2S_{y2} determines the maximum contact pressure, p_0, at which the "weaker" material yields first. For cylindrical contact as given by Green,[31] $C(\nu) = 1.164 + 2.975\nu - 2.906\nu^2$, for $\nu > 0.1938$. Hence, at yielding onset, p_o is replaced by the product

$$CS_y = \min\left\{C_1S_{y1}, C_2S_{y2}\right\} \tag{5}$$

to provide the critical parameters. Herein, the values C_1 and S_{y1} represent the properties of the cylinder, where C_2 and S_{y2} represent the properties of the block. Based on Table 1, ALLOY 800H is the weaker material that yields first both at 20 °C and 800 °C, having smaller CS_y values of 276 MPa and 170 MPa, respectively. These values are used to calculate the critical half-contact width, b_c, and the critical load per unit length, P_c/L , according to Green[31]

$$b_c = \frac{2RCS_y}{E'} \tag{6}$$

$$\frac{P_c}{L} = \frac{\pi R(CS_y)^2}{E'} \tag{7}$$

By substituting equation (7) into equation (4), the critical interference is

$$\begin{aligned}\omega_c = {} & \frac{R(CS_y)^2(1-\nu_1^2)}{E'E_1}\left[2\ln\left(\frac{2E'}{CS_y}\right) - 1\right] \\ & + \frac{R(CS_y)^2(1-\nu_2^2)}{E'E_2}\left[2\ln\left(\frac{dE'}{RCS_y}\right) - \frac{\nu_2}{1-\nu_2}\right]\end{aligned} \tag{8}$$

For the material properties and the depth of the block ($d = R$) herein, the critical interference, the critical load per unit length, and the critical half-contact width for different material schemes at 20 °C and 800 °C are given in Table 2. When the material of the cylinder is ALLOY 617 and the material of the block is ALLOY 800H at 20 °C, $\omega_c = 0.0354$ mm, $b_c = 2.43$ mm, and $P_c/L = 1.05 \times 10^6$ N/m. When the materials are exchanged, $\omega'_c = 0.0356$ mm, while b_c and P_c/L remain the same. (Note that the prime superscript on ω'_c indicates ALLOY 800H being the cylinder while ALLOY 617 being the block and subscript T indicates the elevated temperature of 800 °C.) When the temperature is elevated to 800 °C, the three critical values decrease because of the change of the properties at higher temperatures. Note that critical interferences are very close to each other at the same temperature, so either one could have been used for normalization. Regardless, ω_c, b_c, P_c/L and ω_{cT}, b_{cT}, P_{cT}/L are used to normalize the forthcoming room and high temperature results, respectively.

In this work, the values of the vertical interference are integer multiples of the critical one, namely $1^*\omega_c$, $2^*\omega_c$, $3^*\omega_c$, etc. The amplitude of the horizontal displacement is always kept to be equal to the critical interference, $1^*\omega_c$. In this way, the results are readily nondimensionalized and they can be applied to both macroscopic and microscopic contacts. In this displacement-controlled simulation, the vertical interference and the horizontal displacement, ω and δ, are the inputs, while the normal and tangential forces at the contact, P and Q, are outputs.

Table 2. The critical values for different material schemes and different temperatures.

Temperature	Cylinder material	Block material	Critical interference (μm)	Critical load per unit length (MN/m)	Critical half-contact width (mm)
20°C	ALLOY 617	ALLOY 800H	$\omega_c = 35.4$	$P_c/L = 1.053$	$b_c = 2.432$
	ALLOY 800H	ALLOY 617	$\omega'_c = 35.6$		
800°C	ALLOY 617	ALLOY 800H	$\omega_{cT} = 24.5$	$P_{cT}/L = 0.532$	$b_{cT} = 1.998$
	ALLOY 800H	ALLOY 617	$\omega_{cT}' = 24.8$		
20°C	Steel	Steel	$\omega^*_c = 926.7$	$P^*_c/L = 38.73$	$b^*_c = 14.88$

Mesh convergence

A 2D plain strain element (PLANE183) is used in ANSYS 17.1 to model the contact. The total mesh consists of 66,383 elements, where the mesh in contact area is refined with the element length size of 8×10^{-5}R. One-hundred contact elements are defined on each side of contact. Stiff springs are attached to these elements and activated once penetration is incipient. This is intrinsically handled by the ANSYS contact and target elements, CONTA172 and TARGE169, respectively.

To validate the model, mesh convergence is first performed for the elastic contact (interference ranges from $0.2^*\omega_c$ to $1^*\omega_c$) and the results are compared with those from Hertz contact solution[32] at 20 °C with ALLOY 617 being the material of the cylinder and ALLOY 800H being the material of the block. For the comparison, the normalized interference, ω/ω_c, is the input, where ω_c is calculated by equation (8) (as indicated previously), and thus ω is imposed on the FEA. The theoretical load per unit length, P/L, is calculated from equation (4), while in the FEA simulation P/L is a reaction output. Table 3 presents a comparison of the selected values between theoretical predictions and FEA results for the contact of a half-cylinder of radius R, against a $4\,R \times R$ block in the elastic contact (ω ranges from $0.2^*\omega_c$ to $1^*\omega_c$). The prediction $\sigma_{emax} = p_0/C$ is according to Green,[31] and it is for the weaker material ALLOY 800H. Herein, $R = 0.5$ m, ν_1 and E_1 represent the properties of the ALLOY 617 for the cylinder, while ν_2 and E_2 represent the properties of the ALLOY 800H for the block. As seen in Table 3 for $d/R = 1$, the load per unit length differs by a maximum of 0.53%, the contact width by 2.11%, the maximum contact pressure by 0.274%, and the maximum von Mises stress by 1.19%. With such very small differences, the model and mesh converge have been established for elastic contact. That mesh is also used in the elasto-plastic regime; however, since there is no closed-form solution for elastic-plastic contacts under the combined load of normal and tangential loads, the elements of the mesh are iteratively refined by a factor of two until there is less than one percent difference in the contact width between iterations. Additionally, the region in contact is always confined within the refined mesh (at the vicinity of the origin, as shown in Figure 2). The same mesh convergence is also established for the contact at 800 °C.

Results and discussion

As shown in Figure 3(a), the materials of the cylinder and the block are assigned to ALLOY 617 and ALLOY 800H respectively, and designated as Scheme 1. Then the materials are exchanged in Scheme 2 (Figure 3(b)). The simulations are performed

Table 3. Comparison of selected values between theoretical predictions and FEA results for the contact of a half-cylinder of radius, R, against a $4\,R \times R$ block in elastic contact at 20°C.

	Theoretical predictions					FEA results							
Input	Eq. (8)	Eq. (2)	Eq. (4)	Eq. (1)	p_0/C								
			P/L		σ_{emax}			P/L		p_0		σ_{emax}	
ω/ω_c	ω (μm)	b (mm)	(MN/m)	p_0 (GPa)	(GPa)	b (mm)	% diff.	(MN/m)	% diff.	(GPa)	% diff.	(GPa)	% diff.
0.2	7.08	1.016	0.184	0.115	0.0627	1.037	2.11	0.183	−0.53	0.114	−1.29	0.0619	−1.19
0.6	21.2	1.841	0.604	0.209	0.114	1.877	1.94	0.601	−0.42	0.207	−0.76	0.1130	−0.46
1	35.4	2.432	1.053	0.276	0.150	2.436	0.20	1.050	−0.31	0.274	−0.55	0.1498	−0.13

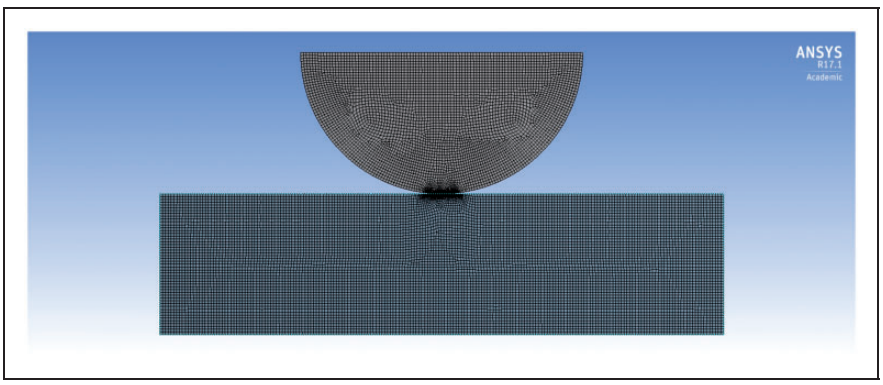

Figure 2. Finite element model in ANSYS 17.1.

for both schemes at room temperature first, and then for scheme1 at 800 °C. Because the fretting damage on the block is of interest here, results of Scheme 1 with the weaker material being the block, will be shown in the following. Meanwhile, the results of Scheme 2 will help to understand the junction growth.

The results of finite element model described above are presented for normalized vertical interference, $\omega^* = \frac{\omega}{\omega_c}$, ranging from 1 (the limit of the elastic regime) to 3 (in the elastic-plastic regime). Two different frictional coefficients are applied, 0.3 and 1. In order to describe the oscillatory horizontal displacement, load steps are used. As shown in Figure 4, Step 0 represents the start of the horizontal load just after the vertical interference is applied. Each increment of step represents a sliding distance of $0.1*\omega_c$. It takes 40 steps to finish one cycle of loading. Due to the computational burden (13 h for a single simulation on a 3 GHz Intel Xeon PC Workstation), the maximum cycle of horizontal displacement investigated in this work is set to three cycles. The following convention of notation is used to signify the location and the cycle number. Points A, B, C, D signify $\delta = (0, 1, 0, -1)\omega_c$ respectively, and $n = 1,2,3$ specify the cycle number. For example, A3 represents the inception of the third cycle, where $\delta = 0*\omega_c$.

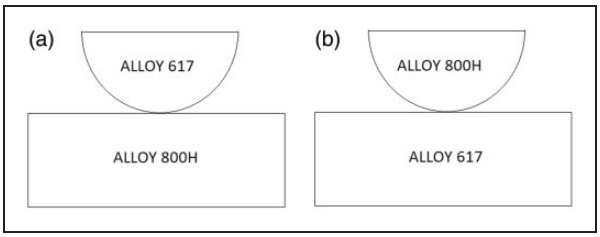

Figure 3. Material schemes for the fretting model: (a) Scheme 1; (b) Scheme 2.

The evolution of von Mises stresses

Figure 5 illustrates the evolution of the von Mises stresses for Scheme 1 at $1*\omega_c$ interference for three cycles of horizontal loading with $\mu = 1$, at 20 °C. After pure normal contact between the cylinder and block is made, i.e. at the inception of the cylinder sliding to the right (location A1 in Figure 4), the maximum von Mises stress in the cylinder and the block reaches $S_{y2} = 150$ MPa (see Figure 5(a)), which equals to the yield strength of ALLOY 800H, being the weaker material of the block. The maximum von Mises stress in the cylinder is 153 MPa, which is slightly larger than that in the block (but still smaller than its yield strength of 322 MPa). Theoretically, according to Green,[31] the maximum von Mises stress in the cylinder for this case, $\sigma_{emax1} = p_0/C_1 = 153$ MPa ($p_0 = S_{y2}C_2$, as mentioned in a previous section), agrees well with the FEA results. Then, from position A1, the cylinder starts to move to the right. Figure 5(b) shows the distribution of the von Mises stresses when the cylinder reaches the rightmost position (location B1 in Figure 4). For the cylinder, even with the tangential force, the material does not yield. Hence, the von Mises stress keeps increasing where the maximum value reaches 280 MPa. For the block, since the von Mises stress has reached the yield strength after the normal contact, there is no increase in the maximum value, but the plastic area (represented by the orange color in Figure 5) gets larger and reaches the surface. As the sliding proceeds back and forth, the region with large von Mises stresses appears at the two edges of the contact, as shown in Figure 5(c) and (d). Therefore, cracks are expected

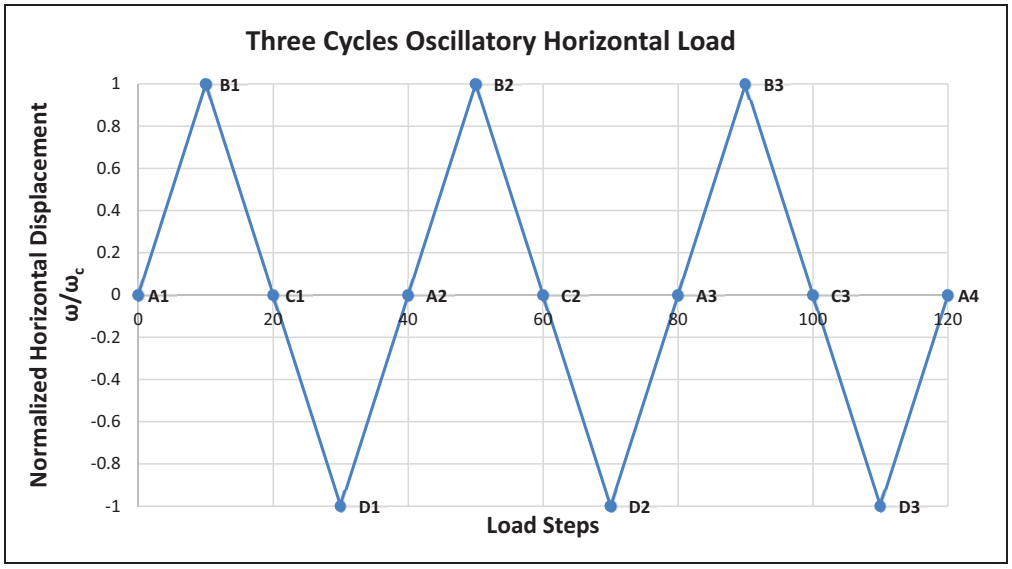

Figure 4. Load stepping of three cycles oscillatory horizontal load.

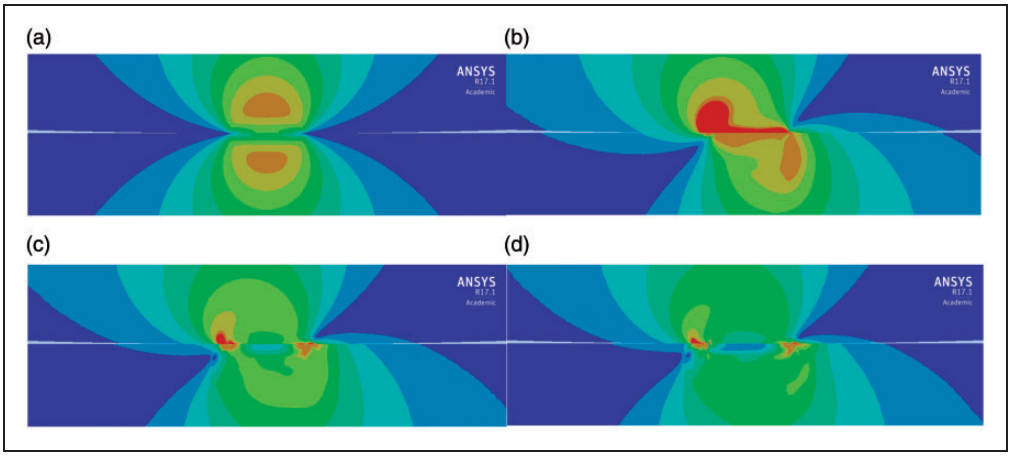

Figure 5. The distribution of von Mises stresses at $1^{*}\omega_c$ interference for three cycles of horizontal loading with $\mu=1$ for Scheme 1 at 20 °C: (a) at load step A1 (shown in Figure 4), max = 150 MPa; (b) at load step B1, max = 270 MPa; (c) at load step A2, max = 250 MPa; (d) at load step A4, max = 230 MPa.

to initiate and propagate most likely at the two edges of the contact during the fretting motion. For the cylinder, although there is no plastic deformation, the large von Mises stresses at the two edges of the contact are likely to introduce fretting fatigue. For the block, the cumulative plastic deformations at two edges of the contact are likely to introduce fretting wear and also fretting fatigue.

The maximum von Mises stress in the cylinder never reaches the yield strength of ALLOY 617 during the three cycles of loading at $1^{*}\omega_c$ interference. Since the maximum value stabilizes after one cycle of loading, the cylinder in this case is presumed to never yield. In order to find the interference at which the cylinder will yield in Scheme 1, up to 10 critical interferences cases with one cycle of horizontal loading have been simulated. However, the results show that the cylinder never yields. At $7^{*}\omega_c$ interference, the maximum value of the von Mises stress is 290 MPa, which is about 4% increase while the interference increases seven times. As the interference increases to $10^{*}\omega_c$ interference, the maximum von Mises still stays at 290 MPa. It can be explained that the effect of plasticity decreases the rate of the load per unit length growth significantly, with respect to the growth of the applied interference, as the contact approaches the fully plastic regime. Therefore, it can be postulated that at room temperature for Scheme 1, the cylinder of material ALLOY 617 is very ''strong'' or ''hard'' yield when it is in contact with block of material ALLOY 800H. Similar results for the block of material ALLLOY 617 in Scheme 2 have been found, but are not reported for brevity.

The distribution of the plastic strain

When the von Mises stresses in the block of material ALLOY 800H first reach the yield strength and fretting is in the elastic-plastic regime (Scheme 1), there are plastic strains in the block, which are indicated by the equivalent plastic strain, ε_p. Figure 6 shows the distribution of ε_p at the region of contact after three cycles of horizontal loading have completed, at different interferences and COFs. In all the three cases, the maximum ε_p is located at the two edges of contact on the block, which coincides with the location of the maximum von Mises stress. That is consistent with the direct correspondence between stress and strain. Because the von Mises stress in the cylinder does not reach the yield strength, as discussed in the previous section, there are no plastic strains in it. Hence, all the plastic strains seen in Figure 6 are in the block.

Figure 6(a) illustrates the plastic strain distribution at $1*\omega_c$ interference with $\mu = 1$. Since there is no plastic strain under surface after the normal loading (only at one point the von Mises stress reaches the yield strength), the plastic strain is confined near the surface to absorb the work generated by the friction force. As the interference increases to $3*\omega_c$ (Figure 6(b)), the plastic strain distribution changes. Because the region under the surface reaches plasticity in a much larger area (details provided by Jackson and Green[13]), the plastic strain spreads to a deeper and wider region under the surface. Consequently, the larger region absorbs the damage manifested by a deeper scar. As a result, the maximum ε_p (located at the edges) is relatively smaller at larger interference. In other words, as the contact produces more permanent damages, there is less plastic strain at the edges, i.e. at the location where the failure, as postulated in the previous section, is most likely to show up. Evident from the maximum values in Figure 6(b) ($\mu = 1$) and Figure 6(c) ($\mu = 0.3$), the plastic strain decreases with the drop of the COF, especially at the edges.

In order to understand the progression of the plastic strain, the distribution of ε_p on the surface of the block after each horizontal loading cycle is investigated. Figure 7(a) shows the evolution of the plastic

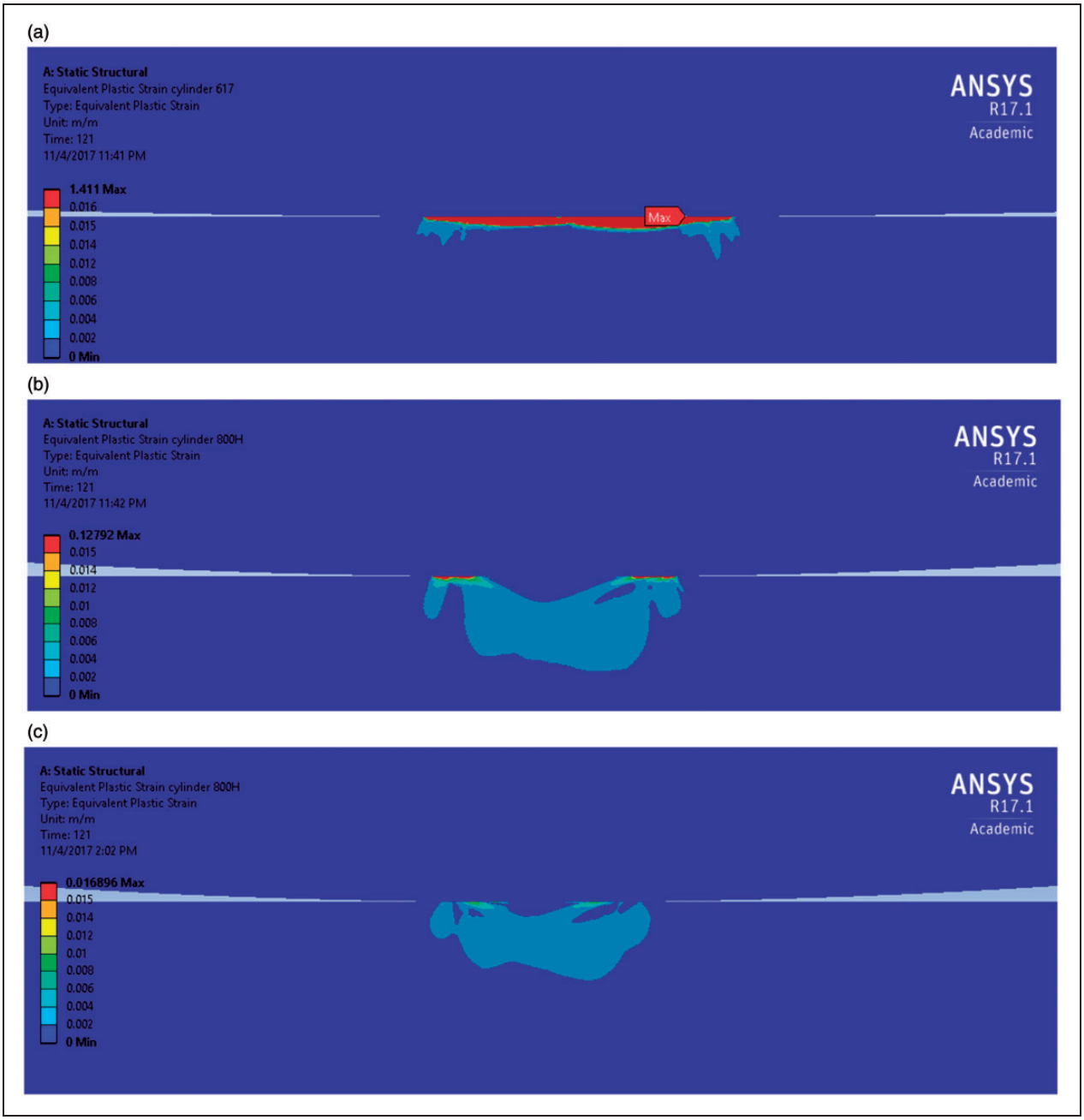

Figure 6. The distribution of the equivalent plastic strain after three cycles of horizontal load near the contacting area for Scheme 1: (a) $1{*}\omega_c$ interference, $\mu = 1$, maximum $\varepsilon_p = 1.41$; (b) $3{*}\omega_c$ interference, $\mu = 1$, maximum $\varepsilon_p = 0.12$; (c) $3{*}\omega_c$ interference, $\mu = 0.3$, maximum $\varepsilon_p = 0.012$.

strain on the surface of the block after three cycles of horizontal loading at $1{*}\omega_c$ interference with $\mu = 1$. The plastic strain keeps increasing after each cycle, and the relative large value locates near the edges of the contact. Outside the initial contacting area ($|X/b_c| > 1$), there are smaller peaks of equivalent plastic strains on each side. These small peaks are caused by the abrupt change of the values of the three normal stresses and shear stress inside and outside the contact area (shown in Figure 7(b)). The abrupt change of the four stresses leads the von Mises stress to reach another peak, which reaches the yield strength as shown in Figure 7(b). The peak of the von Mises stress contributes to the peak of the plastic strain.

The distributions of the plastic strains are asymmetric in Figures 6 and 7. The plastic strains on the right are always larger than those on the left. That is due to the displacement-controlled loading conditions. The normal load during the fretting motion decreases gradually since the block deforms plastically leading to a reduction in the effective resistance to the vertical interference. The cylinder first moves to the right, which leads to larger plastic strains on the right as it experiences a larger normal load.

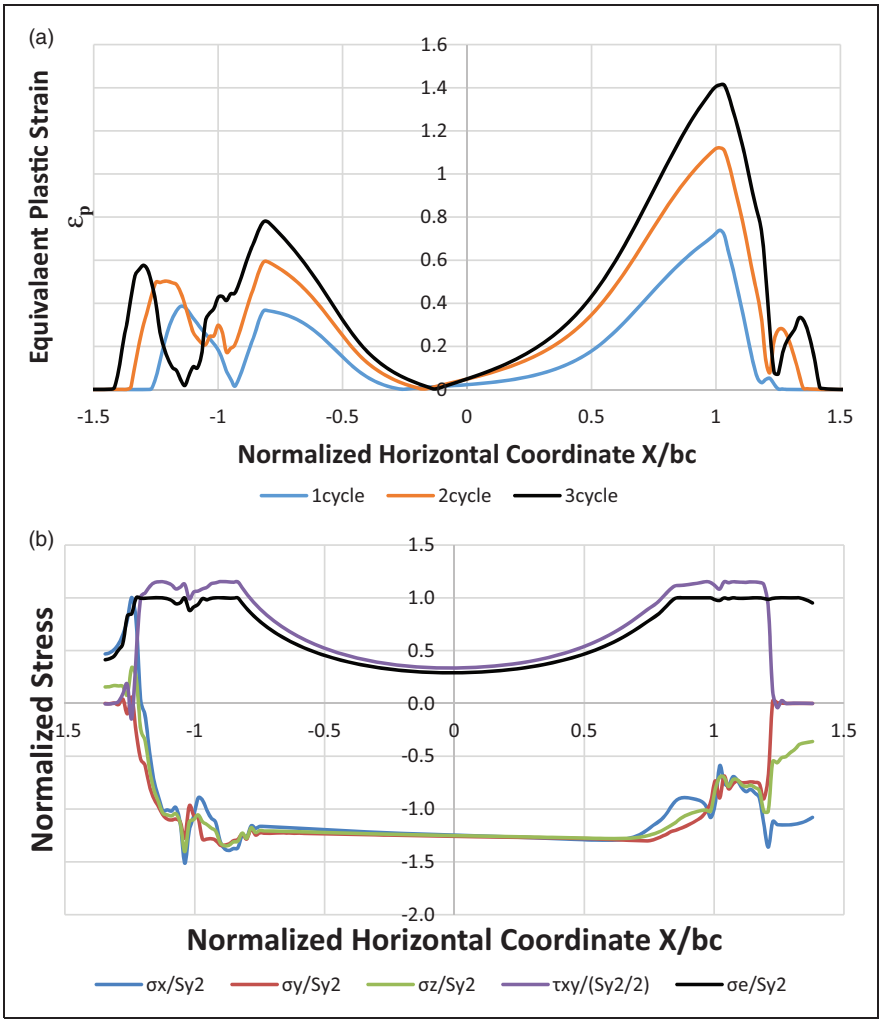

Figure 7. The distribution of the equivalent plastic strain, normalized stresses, and shear stress on the contacting surface of the block at $1*\omega_c$ interference with $\mu = 1$ for Scheme 1: (a) plastic strain; (b) normal stress and shear stress.

Junction growth

Junction growth is the increase of the contacting area, and it is obtained during the fretting motion from FEA code. Figure 8 illustrates the evolution of the half-contact width during the three cycles of horizontal load at $1*\omega_c$ interference with $\mu = 1$ for Scheme 1. It shows that the contact width keeps increasing during the three cycles, but it tends to stabilize. The introduction of the tangential force together with the normal load causes plastic deformation on the surface of the contact. The plastic deformation leads to the junction growth. Since the cylinder is also being flattened, the normal force required to keep the constant interference decreases during the fretting motion. With the decrease of the normal force, the tangential force decreases. When the corresponding von Mises stresses drop under the yield strength, the plastic deformation stabilizes along with the junction growth.

The two edges of the contact keep moving outwards during the fretting motion. However, the contributions to the junction growth, $\Delta b = b - b_{A1}$, of the two edges grow at a different rate as it is evident from Figure 9, which shows the evolution of the contributions to the growth of the two sides at $1*\omega_c$ interference with $\mu = 1$ for both schemes. The variable Δb represents the increase of the absolute value of the horizontal coordinate of the edges of the contact with respect to the values after the pure normal critical interference. For Scheme 1, the right side contributes more than the left side at the first quarter of the cycle, which means the deformation on the right side of the block is more pronounced. When the cylinder turns to the left, the left side starts to contribute more than the right side. At the end of the first cycle, the contributions of the two sides reach almost the same value. According to the results of the Scheme 1, a conclusion could be drawn that the more pronounced junction growth occurs in the same direction of the tangential force experienced by the surface of the deformed body, i.e. the block. When the materials of the two bodies are exchanged, i.e. Scheme 2, the behavior of the junction growth on the two sides reverses, too. In Scheme 2, the left side contributes more to the growth during the first quarter of the cycle, while the right side starts to contribute more

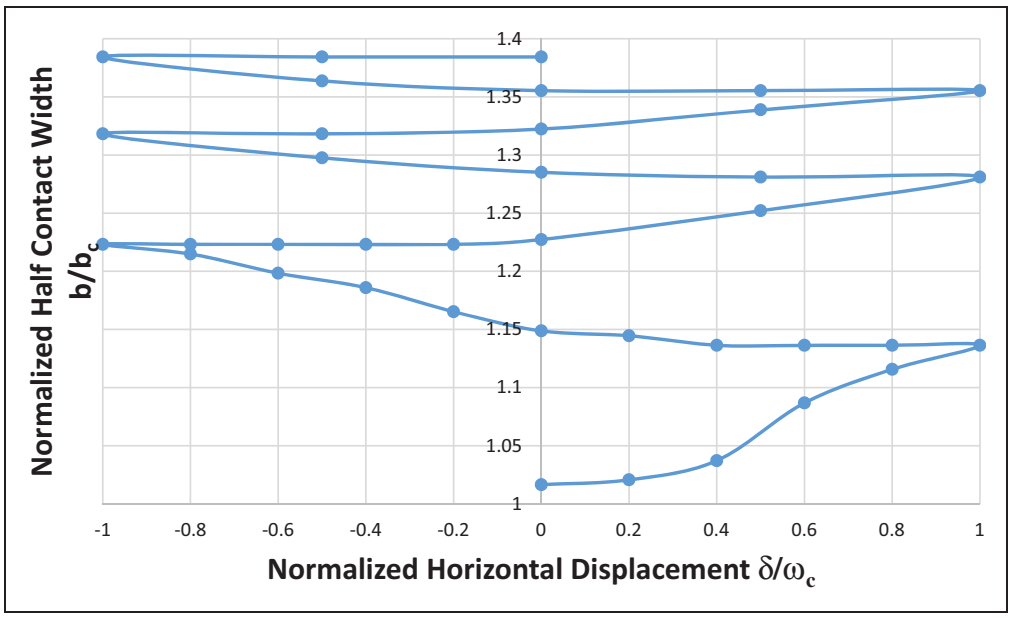

Figure 8. The evolution of the junction growth as indicated by the normalized half-contact width for three cycles of horizontal load at $1^{*}\omega_c$ interference with $\mu = 1$ for Scheme 1.

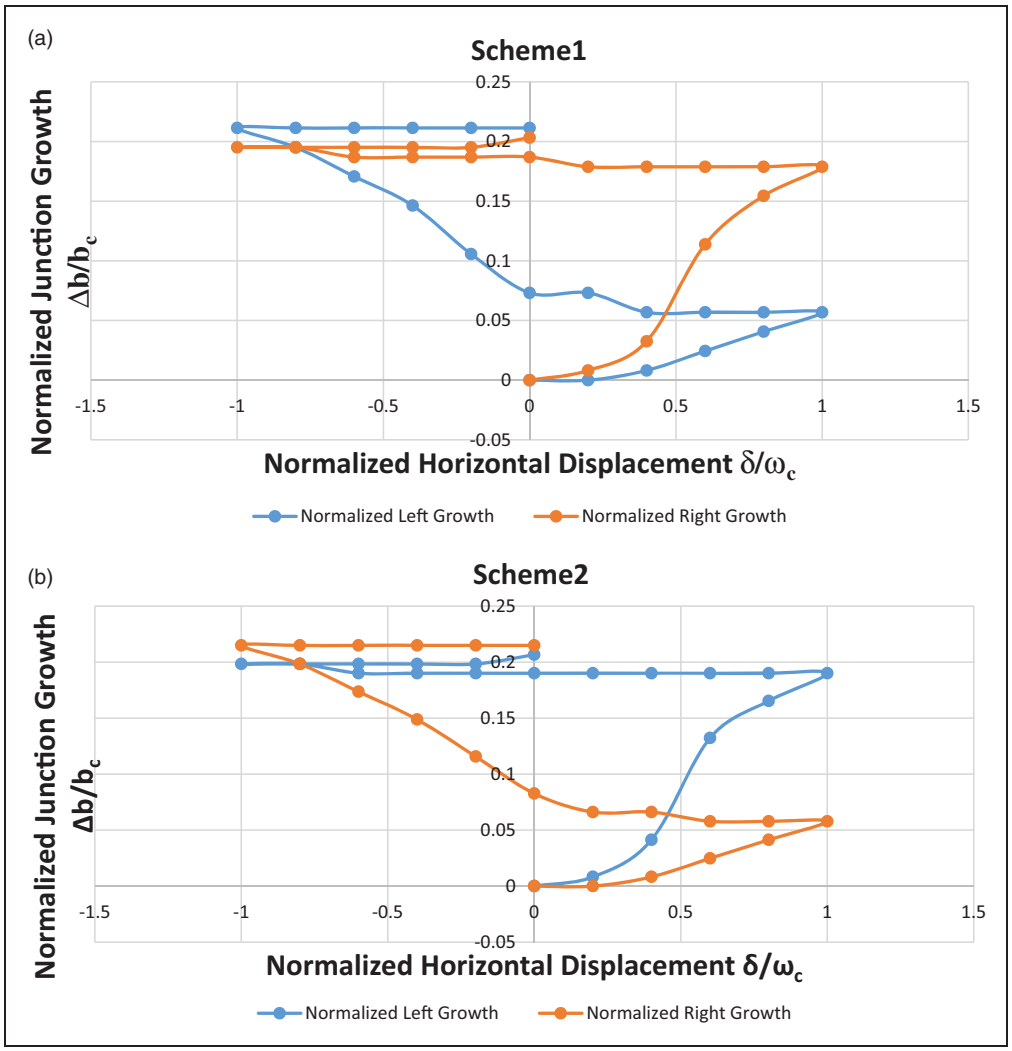

Figure 9. The junction growth as indicated by the normalized half-contact width on the two sides of the contact during the first horizontal cycle at $1^{*}\omega_c$ interference with $\mu = 1$ for different material schemes: (a) material scheme 1; (b) material scheme 2.

after the cylinder turns to the left. The more pronounced growth is in the same direction of the tangential force experienced by the surface of the cylinder, i.e. the weaker material (ALLOY 800H). The conclusion above is further verified. It is also consistent with the conclusion of Brizmer et al.[16] that in the contact between a deformable sphere and a rigid flat under full stick condition, the junction growth is in the same direction of the tangential force experienced by the sphere.

The development of the tangential force

The development of the tangential force per unit length during the fretting motion is recorded. Figure 10(a) depicts the evolution of Q at $1*\omega_c$ interference with $\mu = 1$ for three horizontal loading cycles. That behavior is typically for the initial cycles of the fretting loop according to Walvekar et al.[33] The enclosed area represents the energy loss caused by the fretting motion under the given COF. As the cycle number increases, the maximum tangential force increases, which can be caused by the cumulative plastic deformation on the surface of the block.

Figure 10(b) illustrates the evolutions of the tangential force during three cycles of loading at $3*\omega_c$ interference with different COFs. When the COF is relatively small ($\mu = 0.1$ and 0.2), the loop stabilizes after the first cycle. Additionally, the effective COF ($\mu_e = Q/P$), stabilizes at the value of the COF applied, $\mu = 0.1$ and 0.2, respectively. It is attributed to the full slip contact conditions (as indicated by ANSYS) at the right and left most positions. When the COF increases to $\mu = 0.3$, the loop does not stabilize after three cycles, but tends to stabilize after sufficient number of cycles. Therefore, the fretting loop stabilizes at the initial few cycles of loading for small COFs. The larger the COF, the larger of

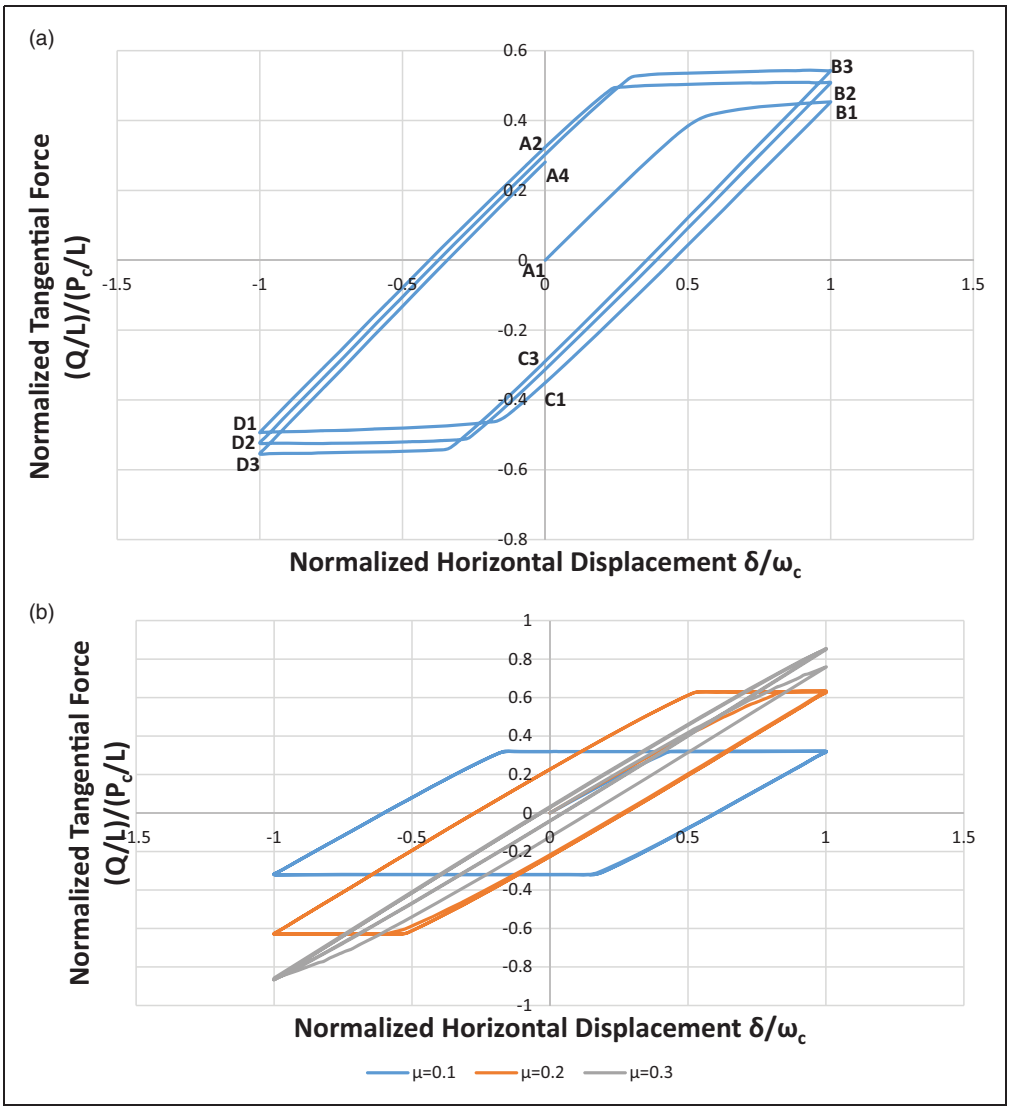

Figure 10. The development of the normalized tangential force during three cycles of the horizontal loading for Scheme 1: (a) $1*\omega_c$ interference with $\mu = 1$; (b) $3*\omega_c$ interference with different COFs.

the number of loading cycles that the loop needs to stabilize.

The scars on the block

As the fretting motion proceeds, a scar is generated on the surface of the flat block. The scar can be visualized by the deformed curve of that surface. Figure 11 shows the deformed curve at $3*\omega_c$ interference with $\mu = 1$ right after the interference is applied for Scheme 1. The curve is identical in shape to that of an elastic half-space with line loading, as given by Johnson.[32] When the curve near the contact is zoomed in (see the inset in Figure 11), the indentation caused by the interference becomes clearly visible. The normalized deformation at the center of the surface of the block is about $1.6*\omega_c$, which is larger than half of the applied interference, $3*\omega_c$. That is caused by the plastic deformation on the block, while the cylinder deforms entirely elastically.

The scar grows during the oscillatory horizontal loading. Figure 12 depicts the deformed curves of the surface of the contact region at $3*\omega_c$ interference after three cycles of loading with $\mu = 0.3$ (under partial slip and partial stick, as indicated in ANSYS) and $\mu = 1$ (under full stick, as indicated in ANSYS). For $\mu = 0.3$, the scar (shown in Figure 12) is deeper than the original one (shown in the inset of Figure 11)

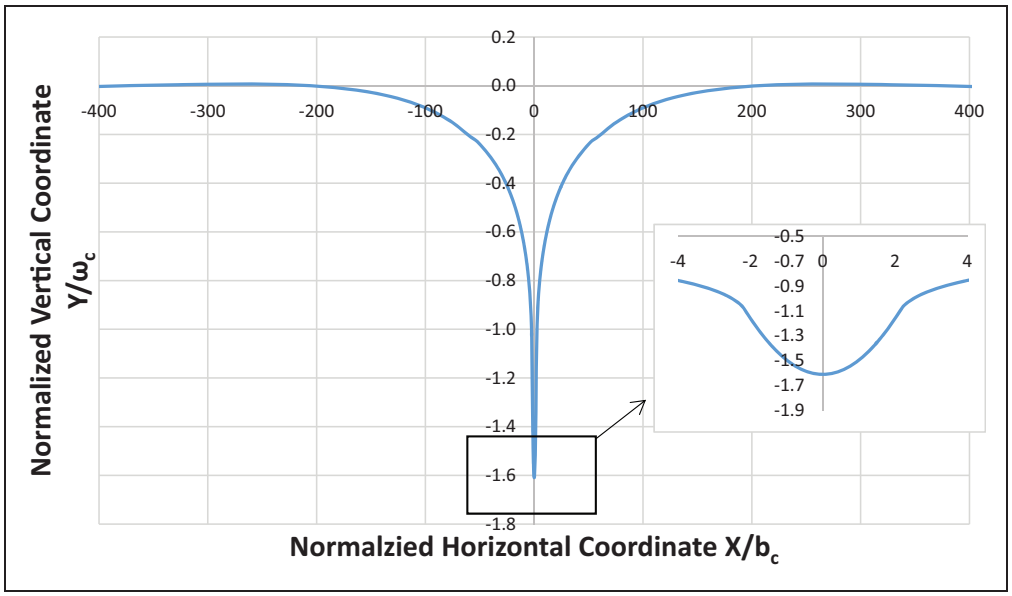

Figure 11. The curve of the surface of the block after $3*\omega_c$ interference.

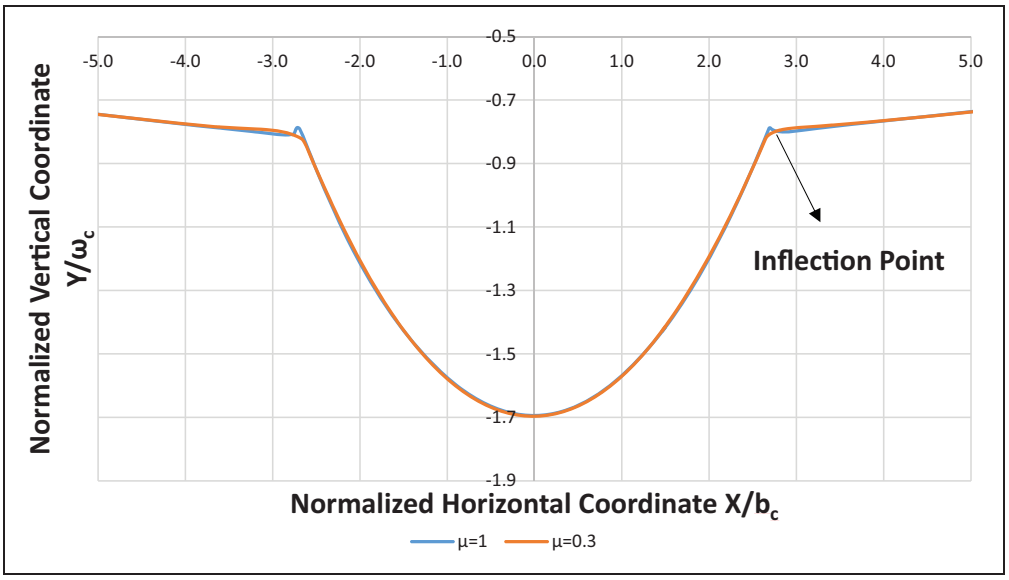

Figure 12. The scars on the surface of the block at $3*\omega_c$ interference after three cycles of load.

right after the interference is applied. It can be understood by the decrease of the normalized Y-axis of the center of the surface on the block from -0.16 (shown in Figure 11) to -0.17. For $\mu = 1$, pileup shows up at near the inflection point of the curve. According to the results above, the pileup occurs at the edges of the indentation with a sufficiently large COF, especially in the case of the full stick condition. The abrupt change of the curvature or pileup will further produce the large von Mises stress and plastic deformation at the corresponding position of the contact.

The influence of the temperature

The results above are acquired at 20 °C. In this section, results at 800 °C are obtained and compared with those at 20 °C. Firstly, the absolute horizontal and vertical displacements are kept the same at 20 °C and 800 °C to show the influence of the temperature. Secondly, the normalized horizontal and vertical displacements at 800 °C (ω/ω_{cT} and δ/ω_{cT}) are kept to be equal to those at 20 °C (ω/ω_c and δ/ω_c) to show the function of normalization.

Table 4 shows the results at the two temperatures with the same absolute displacements after one cycle of horizontal displacement with $\mu = 1$. With the increase of the temperature, the plastic strain increases as a result of the decrease of the elastic modulus, E. Meanwhile, the tangential force, normal force, and the maximum von Mises stress in the cylinder decrease. It is attributed to the decrease of the yield strength of the materials at elevated temperature.

Figure 13 shows the junction growth during one cycle of horizontal displacement at $1^*\omega_c$ interference for 20 °C, and $1^*\omega_{cT}$ interference for 800 °C with the same normalized displacement input and the same COF, $\mu = 1$. The results are also compared with the normalized junction growth when the two bodies consist of identical steel materials, obtained by Yang and Green.[22] The evolutions of the normalized contact width for the three cases are essentially the same. Additionally, based on Figure 14, the evolutions of the normalized tangential force in the three conditions

Table 4. Different results at 20°C and 800°C after $1^*\omega_c$ interference and one cycle of horizontal displacement, whose magnitude is $1^*\omega_c$, with $\mu = 1$ for Scheme 1.

Temperature	Plastic strain, ε_p	Normalized tangential force per unit length, $(Q/L)/(P_c/L)$	Normalized normal force per unit length, $(P/L)/(P_c/L)$	Normalized maximum von Mises stress in cylinder, σ_{e1}/S_{y2}
20°C	0.74	0.54	1.14	2.0
800°C	0.83	0.34	0.82	1.4

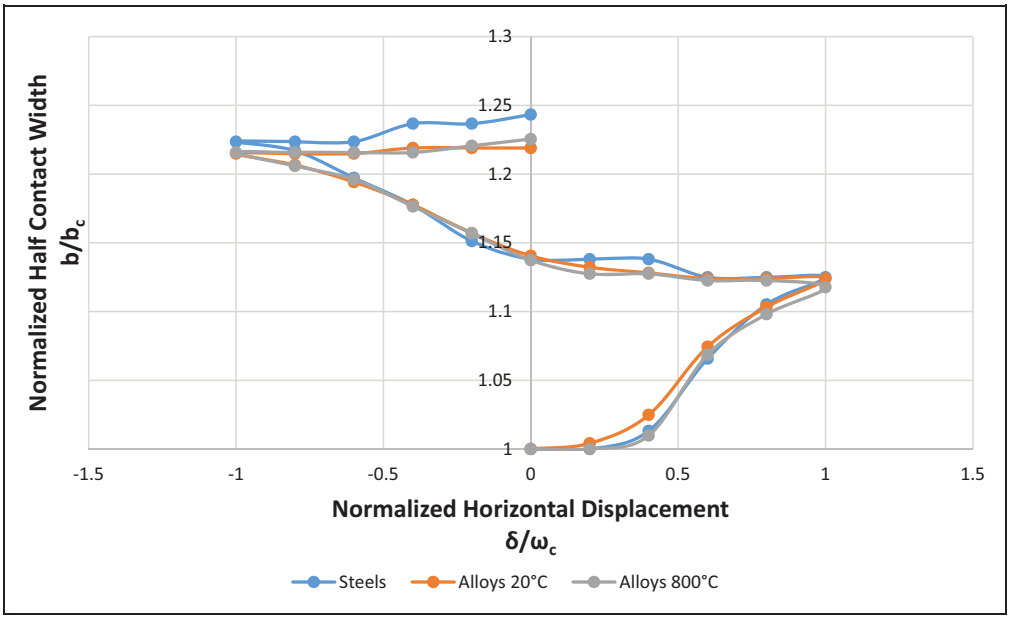

Figure 13. The evolution of the junction growth as indicated by the normalized half-contact width during one cycle of horizontal displacement at $1^*\omega_c$ interference with the same normalized displacement input, $\mu = 1$. Note that b_c and ω_c are taken from Table 1 corresponding to 20 °C or 800 °C, or table from Yang and Green[22] for the steel case.

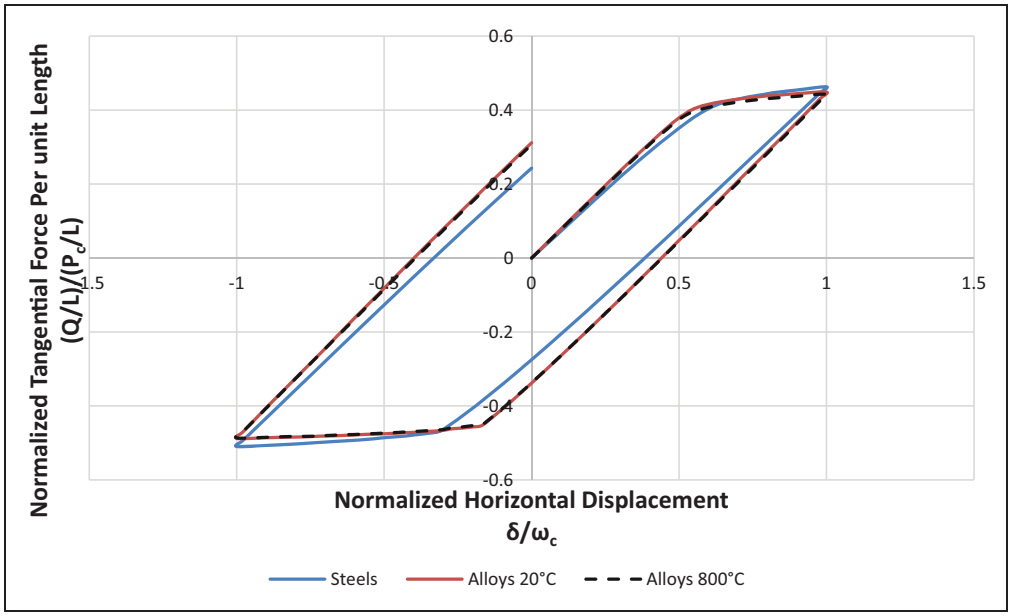

Figure 14. The evolution of the normalized tangential force during one cycle of horizontal displacement at $1^{*}\omega_c$ interference with the same normalized displacement input, $\mu = 1$. Note that b_c, P_c/L, and ω_c are taken from Table 1 corresponding to 20 °C or 800 °C, or table from Yang and Green[22] for the steel case.

are also very close. The good agreement of the normalized contact widths and the tangential forces demonstrates the effectiveness of the normalization even though the critical values of the alloys and steel (see Table 2) are about an order of magnitude different (where also CS_y is much larger for steel, see Table 1). It means that the normalized results of the fretting model for different material properties are effectively the same when normalized. It is suggested, therefore, that the results in this work may be applied to the fretting between materials that are different from those investigated in the current work.

Conclusion

This work presents a 2D plane strain finite element fretting model of a half-cylinder in contact with a block. The materials of the two bodies are ALLOY INCOLOY 800H and ALLOY INCONEL 617. The fretting model is displacement controlled, where it is loaded with an interference first, and then a reciprocating horizontal displacement is applied to the top of the half-cylinder. Different COFs are used in the model. Several conclusions are drawn.

1. During the oscillatory tangential loading, the two contact edges tend to experience the largest von Mises stress. It is, therefore, postulated that cracks and fatigue are most likely to initiate and propagate at the contact edges. Between alloys 800H and 617, the latter is "harder" or "stronger," and in the current investigation it never yielded.
2. The largest plastic strain shows up at the edges, too. The plastic deformation on the surface of the cylinder is not perfectly symmetric about the origin point, where it is slightly larger on the right, which is the direction of the initial motion. This is attributed to the decreasing normal force necessary to maintain a prescribed interference.
3. Due to the plastic deformation of the surfaces, junction growth is found. The more pronounced growth on the two edges is in the same direction of the tangential force experienced by the surface of the deformed body. This conclusion agrees with the results of Brizmer et al.[16] whose model is the contact between a deformable sphere and a rigid flat under full stick condition.
4. The fretting loop (i.e. the development of the tangential force versus fretting motion) for the initial few cycles of loading is found, which is similar to that found experimentally by Courtney-Pratt and Eisner.[3]
5. There are abrupt changes of the curvature at the edges of the indentation on the surface. When the COF is large enough to reach the fully stick condition, pileup will appear at the position of the abrupt change.
6. The temperature elevation causes the increase of the plastic strain and the decrease of the tangential force, normal force, and the maximum von Mises in ALLOY 617.
7. The current normalization scheme has proven to be effective to generate results for various material properties.

Declaration of Conflicting Interests

The author(s) declared no potential conflicts of interest with respect to the research, authorship, and/or publication of this article.

Funding

The author(s) disclosed receipt of the following financial support for the research, authorship, and/or publication of this article: This research was supported by the Department of Energy under Project 2506U87, Award RH452.

References

1. Slack TS, Leonard BD and Sadeghi F. Estimating life scatter in fretting fatigue crack initiation. *Tribol Trans* 2013; 56: 531–535.
2. Mei JN, Xue F, Huang L, et al. Finite element analysis of fretting wear for nuclear Inconel 690 Alloy. *Adv Mater Res* 2013; 772: 77–82.
3. Courtney-Pratt J and Eisner E. The effect of a tangential force on the contact of metallic bodies. *Proc R Soc Lond A* 1957; 238: 529–550.
4. Tabor D. Junction growth in metallic friction: The role of combined stresses and surface contamination. *Proc R Soc Lond A* 1959; 251: 378–393.
5. Parker R and Hatch D. The static coefficient of friction and the area of contact. *Proc Phys Soc B* 1950; 63: 185.
6. Leonard BD, Sadeghi F, Evans RD, et al. Fretting of WC/aC: H and Cr2N coatings under grease-lubricated and unlubricated conditions. *Tribol Trans* 2009; 53: 145–153.
7. Leonard BD, Sadeghi F, Shinde S, et al. A novel modular fretting wear test rig. *Wear* 2012; 274: 313–325.
8. Warhadpande A, Leonard B and Sadeghi F. Effects of fretting wear on rolling contact fatigue life of M50 bearing steel. *Proc IMechE, Part J: J Engineering Tribology* 2008; 222: 69–80.
9. Kim D-G and Lee Y-Z. Experimental investigation on sliding and fretting wear of steam generator tube materials. *Wear* 2001; 250: 673–680.
10. Kim I-S, Hong J-K, Kim H-N, et al. Wear behavior of steam generator tubes in nuclear power plant operating condition. In: *Proceedings of transactions of the 17th international conference on structural mechanics in reactor technology (SMiRT 17)*, Prague, Czech Republic, 2017, pp.D04–05.
11. Zhang X-Y, Liu J-H, Cai Z-B, et al. Experimental study of the fretting wear behavior of Incoloy 800 alloy at high temperature. *Tribol Trans* 2017; 60: 1110–1119.
12. Kogut LEI. Elastic–plastic contact analysis of a sphere and a rigid flat. *ASME J Appl Mech* 2002; 69: 657–662.
13. Jackson RL and Green I. A finite element study of elasto-plastic hemispherical contact against a rigid flat. *Trans ASME-F-J Tribol* 2005; 127: 343–354.
14. Tsukizoe T and Hisakado T. On the mechanism of contact between metal surfaces: Part 2—The real area and the number of the contact points. *J Lubr Technol* 1968; 90: 81–88.
15. Sharma A and Jackson RL. A finite element study of an elasto-plastic disk or cylindrical contact against a rigid flat in plane stress with bilinear hardening. *Tribol Lett* 2017; 65: 112.
16. Brizmer V, Kligerman Y and Etsion I. A model for junction growth of a spherical contact under full stick condition. *J Tribol* 2007; 129: 783–790.
17. Chang L and Zhang H. A mathematical model for frictional elastic-plastic sphere-on-flat contacts at sliding incipient. *J Appl Mech* 2007; 74: 100–106.
18. Boucly V, NĂŠlias D and Green I. Modeling of the rolling and sliding contact between two asperities. *J Tribol* 2007; 129: 235–245.
19. Vijaywargiya R and Green I. A finite element study of the deformations, forces, stress formations, and energy losses in sliding cylindrical contacts. *Int J Non-Linear Mech* 2007; 42: 914–927.
20. Gupta V, Bastias P, Hahn GT, et al. Elasto-plastic finite-element analysis of 2-D rolling-plus-sliding contact with temperature-dependent bearing steel material properties. *Wear* 1993; 169: 251–256.
21. Ghosh A, Leonard B and Sadeghi F. A stress based damage mechanics model to simulate fretting wear of Hertzian line contact in partial slip. *Wear* 2013; 307: 87–99.
22. Yang H and Green I. An elasto-plastic finite element study of displacement-controlled fretting in a plane-strain cylindrical contact. *J Tribol* 2018; 140: 041401-1–041401-11.
23. Mohrbacher H, Celis J-P and Roos J. Laboratory testing of displacement and load induced fretting. *Tribol Int* 1995; 28: 269–278.
24. Brandt J, Charron K, Zhao L, et al. Commissioning of a displacement-controlled knee wear simulator and exploration of some issues related to the lubricant. *Proc IMechE, Part H: J Engineering in Medicine* 2011; 225: 736–752.
25. Johnson T, Laurent M, Yao J, et al. The effect of displacement control input parameters on tibiofemoral prosthetic knee wear. *Wear* 2001; 250: 222–226.
26. Lanovaz J and Ellis R. Dynamic simulation of a displacement-controlled total knee replacement wear tester. *Proc IMechE, Part H: J Engineering in Medicine* 2008; 222: 669–681.
27. Shigley JE and Mischke CR. *Mechanical engineering design*. New York: McGraw-Hill, 1989.
28. Jiang Y, Zhang M, Park T-W, et al. An experimental study of self-loosening of bolted joints. *J Mech Des* 2004; 126: 925–931.
29. Kenny P and Johnson S. An investigation of the abrasive wear of mineral-cutting tools. *Wear* 1976; 36: 337–361.
30. Special Metals. *Product handbook of high performance nickel alloys*, http://www.specialmetals.com/assets/smc/documents/pcc-8064-sm-alloy-handbook-v04.pdf.
31. Green I. Poisson's ratio effects and critical values in spherical and cylindrical Hertzian contacts. *Appl Mech Eng* 2005; 10: 451.
32. Johnson KL and Johnson KL. *Contact mechanics*. Cambridge: Cambridge University Press, 1987.
33. Walvekar AA, Leonard BD, Sadeghi F, et al. An experimental study and fatigue damage model for fretting fatigue. *Tribol Int* 2014; 79: 183–196.

Appendix

Notation

b	half-contact width
b_c	critical half-contact width
C	Poisson's ratio parameter
E_1	elastic modulus of the cylinder
E_2	elastic modulus of the block
E'	equivalent elastic modulus
p_0	maximum contact pressure

p_{0c}	critical maximum contact pressure
P/L	normal force per unit length
P_c/L	critical normal force per unit length
Q	tangential force
R	radius of half-cylinder
S_y	yield strength
σ_x	normal stress in the X direction
σ_y	normal stress in the Y direction
ε_p	equivalent plastic strain
ε_x	normal strain in the X direction
ε_y	normal strain in the Y direction
δ	horizontal displacement
μ	coefficient of friction
ω	interference
ω_1	compression of the half-cylinder
ω_2	compression of the centerline of the block
ω_c	critical interference
ω^*	normalized interference, ω/ω_c
ν_1	Poisson's ratio of the cylinder
ν_2	Poisson's ratio of the block

Appendix 1

The interference of a half-cylinder in contact with a block is derived below. According to Johnson[32] (taken from p. 130, and shown in Figure 15(a)), the elastic compression of a cylinder in contact with two elastic bodies is obtained. The compression of the upper part of the cylinder O_1C is

$$\delta_1 = \frac{P}{L}\frac{(1-\nu^2)}{\pi E}\left\{2\ln(4R/b_1) - 1\right\} \tag{9}$$

where the half-contact width b_1 is calculated according to the Hertzian theory

$$b_1^2 = 4PR/(\pi L E_1^*) \tag{10}$$

where E_1^* is the composite modulus of the upper body and the cylinder

$$\frac{1}{E_1^*} = \frac{1-\nu_1^2}{E_1} + \frac{1-\nu^2}{E} \tag{11}$$

Herein, the model is that of a half-cylinder in contact with a block. The top of the half-cylinder is prescribed with a vertical displacement, which is the interference, ω. That interference consists of two parts, the compression of the half-cylinder, ω_1, and the compression of the centerline of the block, ω_2. For ω_1, we assume the equivalent model shown in Figure 15(b). According to equation (9), the compression of the half-cylinder herein is thus equal to the compression of the lower half-cylinder in Figure 15(b)

$$\omega_1 = \frac{P}{L}\frac{(1-\nu_1^2)}{\pi E_1}\left\{2\ln(4R/b) - 1\right\} \tag{12}$$

where b is the half-contact width between the cylinder and the block. For ω_2, according to Johnson,[32] the compression of the centerline of the block is equal to the compression of a half-space under the load of

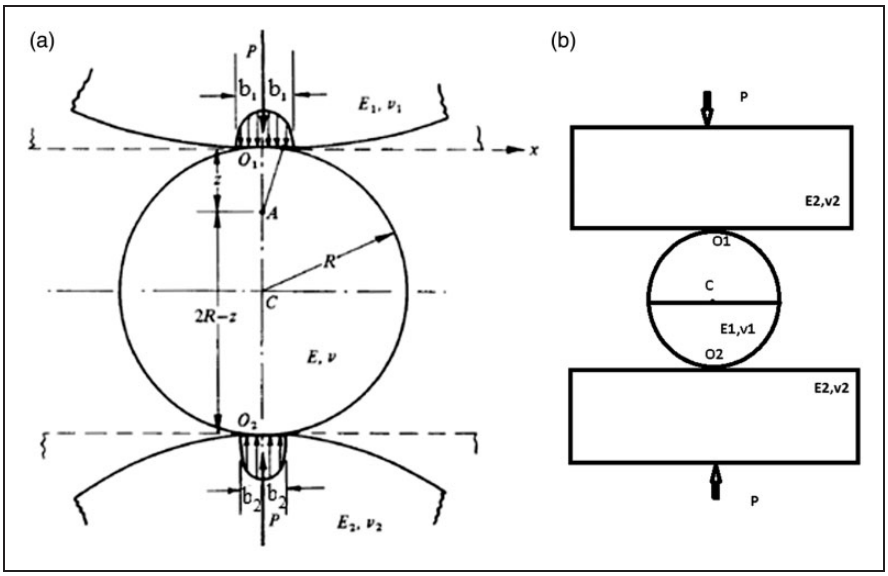

Figure 15. The contact model to derive the compression of the elastic cylinder in contact with an elastic block: (a) the model in *Contact Mechanics* by Johnson (p. 130); (b) the equivalent model of the compression of the half-cylinder herein.

Table 5. Comparison of the critical values between theoretical predictions and FEA results for a half-cylinder of radius is R, in contact with a $4d \times d$ block, of depth, d, at room temperature 20°C for Scheme 1.

	Theoretical predictions					FEA results							
d/R	Eq. (8) ω_c (mm)	Eq. (6) b_c (mm)	Eq. (7) P_c/L (MN/m)	$C_2{}^*S_{y2}$ p_{0c} (GPa)	S_{y2} σ_{emax} (GPa)	b_c (mm)	% diff.	P_c/L (MN/m)	% diff.	p_{0c} (GPa)	% diff.	σ_{emax} (GPa)	% diff.
0.25	31.19	2.432	1.053	0.276	0.1500	2.445	0.52	1.050	−0.28	0.274	−0.56	0.1517	1.11
0.5	33.28	2.432	1.053	0.276	0.1500	2.438	0.25	1.050	−0.27	0.275	−0.50	0.1505	0.34
1	35.37	2.432	1.053	0.276	0.1500	2.436	0.18	1.050	−0.28	0.274	−0.62	0.1498	−0.13
2	37.47	2.432	1.053	0.276	0.1500	2.436	0.18	1.051	−0.24	0.276	−0.10	0.1495	−0.35
4	39.56	2.432	1.053	0.276	0.1500	2.476	1.82	1.050	−0.25	0.275	−0.52	0.1493	−0.48

the Hertzian pressure relative to a point at a depth, d. Hence

$$\omega_2 = \frac{P}{L}\frac{(1-\nu_2^2)}{\pi E_2}\left\{2\ln(2d/b) - \nu_2/(1-\nu_2)\right\} \tag{13}$$

The interference is then the addition of equations (12) and (13)

$$\begin{aligned}\omega = &\frac{P}{L}\frac{(1-\nu_1^2)}{\pi E_1}\left\{2\ln(4R/b) - 1\right\} \\ &+ \frac{P}{L}\frac{(1-\nu_2^2)}{\pi E_2}\left\{2\ln(2d/b) - \nu_2/(1-\nu_2)\right\}\end{aligned} \tag{14}$$

By substituting equation (2) into equation (14), the interference simplifies to

$$\begin{aligned}\omega = &\frac{P}{L}\frac{(1-\nu_1^2)}{\pi E_1}\left\{\ln\left(\frac{4\pi E' R}{P/L}\right) - 1\right\} \\ &+ \frac{P}{L}\frac{(1-\nu_2^2)}{\pi E_2}\left\{\ln\left(\frac{\pi d^2 E'}{RP/L}\right) - \frac{\nu_2}{(1-\nu_2)}\right\}\end{aligned} \tag{4}$$

To verify the assumption of viewing the block as a half-elastic space, different dimensions of the block have been used to compare FEA results with theoretical predictions, where %diff., as given in Table 5, indicates the relative percentage difference between them. According to the table, the FEA results for Scheme 1 and room temperature agree very well with the results calculated according to equations (6) to (8), when the block depth varies from $0.25\,R$ to $4\,R$. Hence, a block whose depth, d, that equals R can safely be regarded as a half-elastic space. Indeed in this work, all reported results are specifically given for that case of $d = R$. Moreover, the nondimensionalized results in this work, can safely be applied to blocks with depths that are about $0.25\,R$ or larger. That proposition conforms to the classical Saint-Venant's principle, which reassures that the critical interferences between two cylinders, as derived by Green[31] in equation (24), and the one derived herein for the contact of a half-cylinder against a block in equation (8), match closely with a mere 1.6% difference.